

Monte Carlo Simulation Study of a Dual-Plate PET Camera Dedicated to Breast Cancer Imaging

Jin Zhang, *Member, IEEE*, Peter D. Olcott, *Member, IEEE*, Angela M. K. Foudray, *Student Member, IEEE*, Garry Chinn, *Member, IEEE*, and Craig S. Levin, *Member, IEEE*

Abstract— We studied the performance of a dual-plate positron emission tomography (PET) camera dedicated to breast cancer imaging using Monte Carlo simulation based on GATE open code software. The PET camera under development has two $10 \times 15 \text{ cm}^2$ plates that are constructed from arrays of $1 \times 1 \times 3 \text{ mm}^3$ LSO crystals coupled to novel silicon-based ultra-thin ($< 300 \text{ }\mu\text{m}$) position-sensitive avalanche photodiodes (PSAPD). With the photodetector configured “edge-on”, incoming photons see effectively 2-cm-thick of LSO with directly measured 3-mm photon depth-of-interaction. Simulations predict that this camera will have $> 10\%$ sensitivity, and detector measurements show $\sim 1 \text{ mm}^3$ intrinsic spatial resolution, $< 12\%$ energy resolution, and $\sim 2 \text{ ns}$ coincidence time resolution. With a breast phantom including breast, heart and torso activity (concentration ratio of 1:10:1, respectively), count performance was studied under varying time and energy windows. We also studied visualization of hot spheres within the breast for $1 \times 1 \times 3 \text{ mm}^3$, $2 \times 2 \times 10 \text{ mm}^3$, $3 \times 3 \times 30 \text{ mm}^3$ and $4 \times 4 \times 20 \text{ mm}^3$ crystal resolutions at different plate separations. Images were reconstructed by focal plane tomography and 3D OS-EM with attenuation and solid angle corrections applied. With an activity concentration ratio of tumor:breast:heart:torso of 10:1:10:1, only the dual-plate PET camera comprising $1 \times 1 \times 3 \text{ mm}^3$ crystals can resolve 2.5-mm tumor spheres with an average peak-to-valley ratio of 1.3 in only 30 seconds of acquisition time.

I. INTRODUCTION

Positron emission tomography (PET) is used for cancer imaging. However, for some dedicated applications such as breast cancer imaging, the traditional full-body PET system has several shortcomings in detection, diagnosis, and staging. In addition to a need for more suitable tracers, there is a need to optimize geometry for breast cancer imaging, reduce the relatively high cost of scanning, and to improve spatial and energy resolution. Scientists and engineers have developed a number of new, portable designs for PET cameras dedicated

to breast cancer imaging in the last several years [1-5]. These designs are generally based on position sensitive photomultiplier tubes (PMT) and relatively large lutetium based scintillation crystals. For example, LSO crystal sizes of $3 \times 3 \times 20 \text{ mm}^3$ [4] and $3.1 \times 3.1 \times 10 \text{ mm}^3$ [5] have been studied with dedicated PET cameras. These camera systems have demonstrated limited spatial resolution of about 3.8 mm [4] and 2.3 mm [5] at the center. To improve performance, we are developing a dedicated breast cancer imaging PET camera based on smaller LSO crystals to achieve around 1 mm spatial resolution with high ($> 10\%$) sensitivity at the center of the field of view (FOV) and directly measured photon interaction depth capability. The camera will have a dual-panel, portable geometry and uses a novel thin ($< 300 \text{ }\mu\text{m}$) semiconductor-based position sensitive avalanche photodiode (PSAPD) from RMD Inc., Watertown, MA. The detector modules of this camera utilize the PSAPDs coupled to 3×8 arrays of $1 \times 1 \times 3 \text{ mm}^3$ LSO crystals, which gives 3 mm direct photon depth-of-interaction (DOI) resolution. Preliminary experimental results with standard PSAPD packaged on ceramic substrate have been reported [6]. We have also studied the new thin PSAPD performance [7] that will be used for the PET camera construction. This PET camera, with a FOV of $15 \times 10 \text{ mm}^2$ with variable plate separation, is expected to achieve $> 10\%$ sensitivity at the center of FOV, and $\sim 1 \text{ mm}^3$ intrinsic spatial resolution, $< 12\%$ energy resolution at 511 keV, and about 2 ns coincidence time resolution. These performance parameters were achieved using the new thin PSAPD devices [7].

In this paper, we present our Monte Carlo simulation results on sensitivity, count rate, and imaging properties of the dual-panel PET camera based on the < 300 -micron-thick PSAPD. We will also compare the imaging performance based on different LSO crystal size. Crystals with sizes of $2 \times 2 \times 10 \text{ mm}^3$, $3 \times 3 \times 30 \text{ mm}^3$ with DOI of 10 mm, and $4 \times 4 \times 20 \text{ mm}^3$ have been simulated with the same dual-panel structure. Lesion visualization and contrast resolution of these LSO-PSAPD PET cameras have been compared. Focal plane tomography (FPT) and maximum-likelihood iterative method were used for the image reconstruction.

II. MATERIALS AND METHODS

We used GATE (Geant4 Application in Tomographic Emission) open source software to perform Monte Carlo simulations of the dual-plate PET camera shown in Fig. 1(a). This camera is constructed with the novel thin PSAPD coupled with $1 \times 1 \times 3 \text{ mm}^3$ LSO crystals shown in Fig. 1(b) and

Manuscript received November 4, 2005. This work was supported in part by R21 CA098691 from NIH-NCI.

J. Zhang was with the Department of Radiology, Stanford University, Stanford, CA. He is now with PerkinElmer Optoelectronics, 2175 Mission College Blvd., Santa Clara, CA 95054, email: jin.zhang@perkinelmer.com.

A.M.K. Foudray is with the Department of Radiology, Stanford University and the Department of Physics, University of California, San Diego, La Jolla, CA, USA (email: afoudray@stanford.edu).

P. Olcott is with the Department of Radiology, Stanford University, Stanford, CA. 94305-5344, USA (email: pdo@stanford.edu).

G. Chinn is with the Department of Radiology, Stanford University, Stanford, CA. 94305-5344, USA (email: gchinn@stanford.edu).

C.S. Levin is with the Department of Radiology, Stanford University, Stanford, CA. 94305-5344, USA (email: cslevin@stanford.edu).

(c). The camera geometry dimensions are shown in Fig. 1(a). Each panel has a height of 15.4cm, width of 10 cm, and a thickness of 2.2 cm. The panel separation is adjustable with a range of 4 cm to 8 cm. Fig. 1(b) shows the layers of LSO coupled to PSAPDs. The PSAPDs are packaged on polyimide (Kapton) “flex” circuits with a total thickness of <math><300 \mu\text{m}</math>. Fig. 1(b) shows that the gamma photons are incident from the right side and the electrical contacts are on the left side for high-voltage (~1700 volts) bias and signal read out. The silicon chip has a physical area of 11x11 mm² with an active area of 8x8 mm², as shown in Fig. 1(c). An 8x3 LSO array is coupled to the center area of the detector. This geometry produces dead area around the detector rim reducing the sensitivity. Some methods to address this issue are under evaluation. Nevertheless, this pet camera showed impressive sensitivity in Monte Carlo simulations.

For the sensitivity simulations, a point source with 100 μCi activity was translated from the center to the FOV edges in order to calculate the sensitivity as a function of position. The noise equivalent counts (NEC) were also simulated with a phantom filling the entire space between the two camera panels. We included activity from a simulated heart and torso. Fig. 2(a) shows the geometry of the phantom and detector system. The heart was a sphere with a 10 cm diameter and the torso was a 30x30x20 cm³ box. NEC is calculated as:

$$NEC = \frac{T^2}{T + S + 2R}, \quad (1)$$

where T, S, and R are true, scatter, and random coincidence event rates. The activity in the breast phantom was increased from 10 μCi up to 2 mCi. In these simulated dual-panel PET studies, the energy window was wide open from 10 KeV up to 1 MeV and the data was processed for different energy and time windows. Energy resolution and time resolution were 12% at 511 keV and 2 ns FWHM, respectively.

For tumor visualization studies, a plane of tumor sources was included in the breast phantom comprising of spheres with various radius, as shown in Fig. 2(b). Each quadrant of the plane consisted of 4 cm, 3.5 cm, 3 cm, and 2.5 cm spheres separated by two times the diameter of the spheres. The activity ratio simulated was 10:1:10:1 for tumor : breast : heart : torso. Table 1 shows the activity concentration and volumes of the background breast, heart, and torso. The tumor source

plane was located the same distance from both camera panels. We also evaluated the resolution performance with different crystals sizes: 1x1x3 mm³, 2x2x10 mm³, 3x3x30 mm³ with 10 mm DOI resolution, and 4x4x20 mm³. The simulation parameters for different crystals are summarized in Table 2.

Focal plane tomography (FPT) [4] and the list-mode ordered subset expectation maximization (OS-EM) [9] were used to reconstruct images (geometry shown in Figure 3).

III. RESULTS

A. Point source sensitivity

Simulation results on sensitivity are shown in Fig. 4 with a point source at the center of the FOV. The sensitivity was plotted versus the time window (Fig. 4 (a) and (b)) and energy window (Fig. 4 (c) and (d)). With the panel separation of 4 cm and 8 cm, the sensitivity saturated at a time window of around 3 ns (Fig. 4 (a) and (b)). With an energy window of 350-650 KeV, the saturation sensitivities were 14.2% and 8.2%, respectively. Fig. 4 (c) and (d) shows that the sensitivity saturated at a energy window range of about 383-639 keV (25%) up to 358-664 keV (30%). The sensitivity increases again at an energy window above ~65% of 511 KeV. This is because the further enlarged energy window includes more low energy scatter events from energy spectrum, as shown in Fig. 4.

To evaluate the sensitivity at different positions, we moved the point source along the y- and z-axis (see Fig. 1 (a)) with a step size of 1 cm. The calculated sensitivity was plotted in Fig. 5 for the panel separation of 4 cm and 8 cm. It is noted that by reducing the panel separation from 8 cm to 4 cm, the sensitivity could be increase by about 80%.

B. Coincident count rates

Fig. 6 shows the NEC, calculated using Eqn. (1), as a function of the activity in the breast phantom with plate separation of 4cm and 8 cm along. The NEC as a function of time and energy window is also plotted. Background from the heart and torso were included.

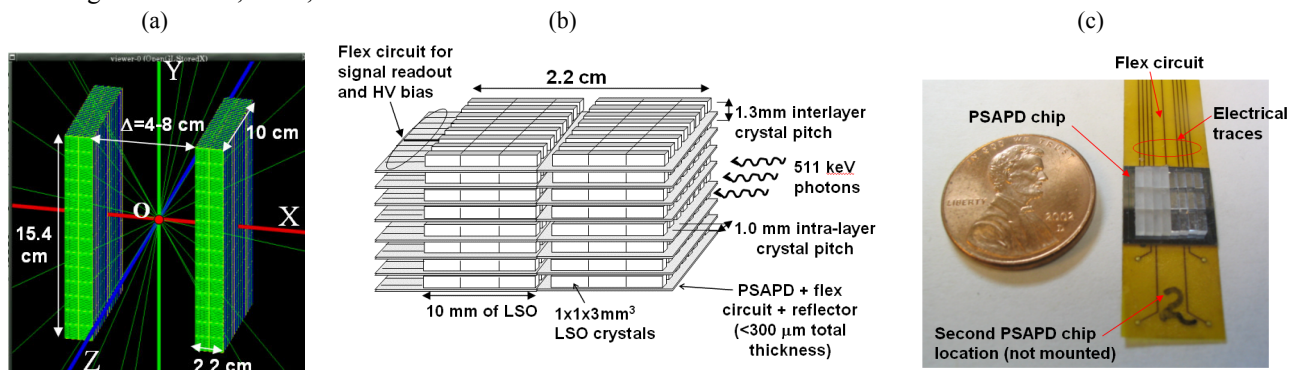


Fig. 1. (a) Dual-panel PET camera geometry based on the novel thin PSAPD. (b) Schematic of the crystal and detector module. (c) An 8x3 array of 1x1x3mm³ LSO crystals coupled to thin PSAPD with only one silicon chip mounted.

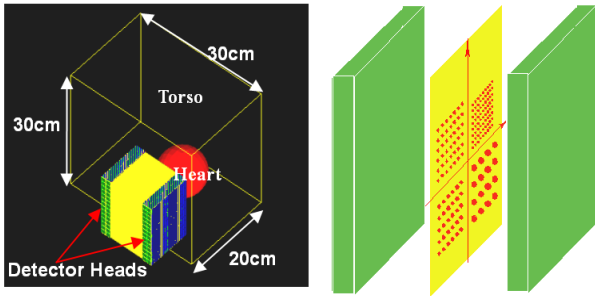


Fig. 2. (left) The breast, heart, and torso phantom. (right) Four quadrants of tumor spheres (2.5, 3.0, 3.5, and 4.0 mm diameter with twice the separation) placed between the plates inside breast tissue. The activity concentration ratio was tumors:breast:heart:torso=10:1:10:1.

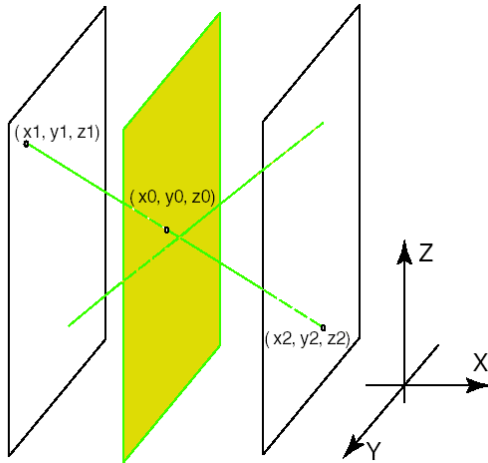


Fig. 3. Schematic of FPT image reconstruction geometry.

TABLE I. CONCENTRATION IN PHANTOMS AND CORRESPONDING VOLUMES

Phantoms	Activity concentration ($\mu\text{Ci}/\text{cm}^3$)	volume (cm^3)	Activities (μCi)
Breast	0.1	$8 \times 15 \times 10 = 1200$ $5 \times 15 \times 10 = 750$ $4 \times 15 \times 10 = 600$	120 75 60
heart	1	523.6	523.6
Torso	0.1	$30 \times 30 \times 20 = 18000$	1800

TABLE II. PARAMETERS USED IN MONTE CARLO SIMULATION FOR DIFFERENT CRYSTAL RESOLUTIONS FOR $15 \times 10 \text{ cm}^2$ PLATES

LSO crystal size (mm^3)	$1 \times 1 \times 3$	$2 \times 2 \times 10$	$3 \times 3 \times 30$	$4 \times 4 \times 20$
Effective thickness (mm)	18 (six layers)	10	30	20
ER at 511 keV (%)	12%	16%	25%	20%
Energy window	450-573	350-650	350-650	350-650
Time resolution	2	2	2	2
Time window	4	4	4	4
DOI resolution (mm)	3	n/a	10	n/a

For 200 μCi activity in the breast tissue compartment, the peak NEC was 2,000 counts/sec at 2-3 ns time window and $\sim 24\%$ energy window. To obtain the best sensitivity and NEC while rejecting scatter and random events, we used a 4 ns time window and 24% energy window to reconstruct images for our dual-panel camera based on the $1 \times 1 \times 3 \text{ mm}^3$ LSO crystals.

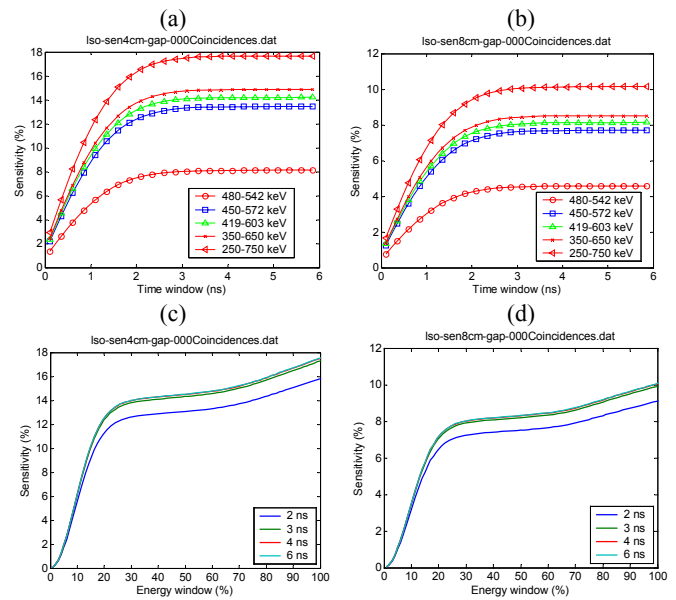


Fig. 4. Sensitivity for a point source at the center of FOV as a function of ((a) and (b)) time window and ((c) and (d)) energy window for panel separation

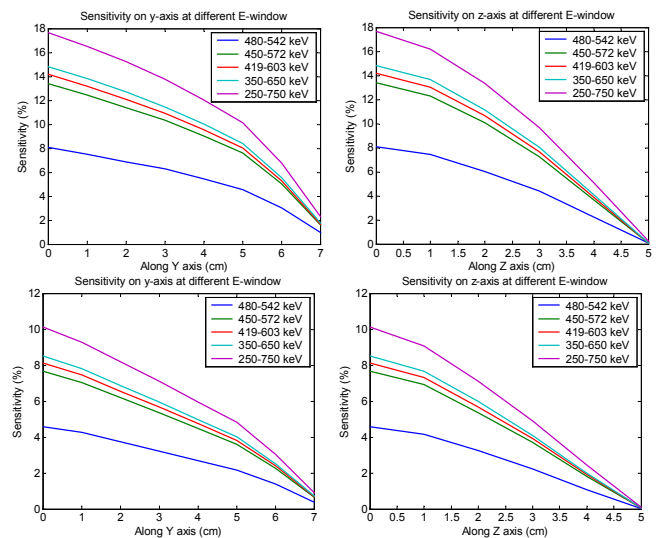


Fig. 5. Sensitivity for a point source translated along the y- and z-axes.

C. Tumor Visualization Study

Focal plane tomography (FPT) was used for most of the image reconstructions presented in this paper (see Figure 3). The left (x_1, y_1, z_1) and right (x_2, y_2, z_2) interaction positions determine the line of response (LOR). The image plane could be placed anywhere between the two detector panels, but the resolution is the best at the foci of the LORs, which should correspond to the tumor source location. The backprojection intercept point (x_0, y_0, z_0) of the LORs on the image plane generates the focal plane image on the y-z plane at x_0 .

Fig. 7 shows the FPT images without any background activity for four simulated systems with crystal resolution of (a) $1 \times 1 \times 3 \text{ mm}^3$ with DOI resolution of 3 mm, (b) $2 \times 2 \times 10 \text{ mm}^3$, (c) $3 \times 3 \times 30 \text{ mm}^3$ with DOI resolution of 10 mm, and (d)

$4 \times 4 \times 20 \text{ mm}^3$. Activity concentration in the sphere sources was $1 \mu\text{Ci}/\text{cc}$. From this figure, we see that the crystal size is directly related to the sphere resolution achieved. Fig. 8 shows the FPT images with only breast phantom present and the tumor:breast activity concentration ratio is 10:1. The 1-D profiles along the sources through the line marked by the arrow in Fig. 9(a) were also plotted. Images with the breast, heart and torso background present were shown in Fig. 9 together with the 1-D profiles along the marked arrows in Fig. 9(a). The acquisition time of the images in Fig. 8 and 9 are all 30 seconds only.

Fig. 10 shows additional FPT reconstructed data with and without heart and torso background activity for (a) 4 cm panel separation with source plane offset by 1 cm and 10:1 tumor:breast concentration ratio, (b) 4 cm panel separation tumor plane at center, but 5:1 tumor:breast concentration ratio, and (c) 8 cm panel separation with tumor plane at center and 10:1 concentration ratio.

We also used the list-mode OS-EM algorithm to compare with the FPT images (Fig. 11). A single iteration with 8 subsets was used to reconstruct the images. We noticed improved image quality with the OS-EM algorithm.

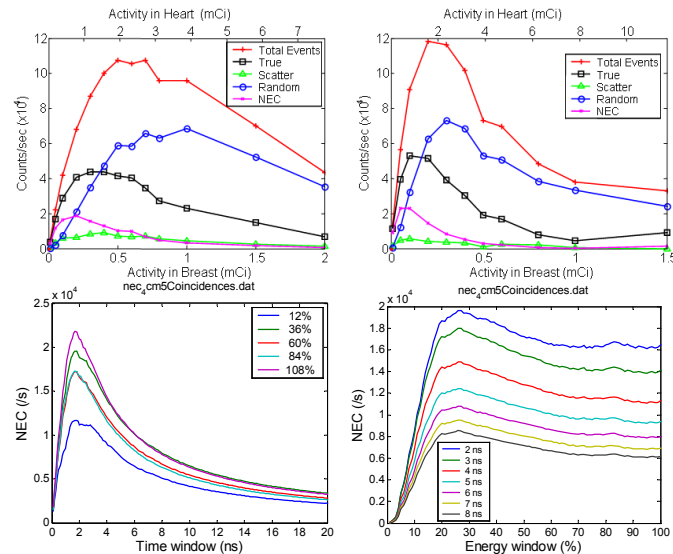


Fig. 6. NEC as a function of the activity in breast (lower x-axis) and heart (upper x-axis) with panel separation of (a) 4 cm and (b) 8 cm. Plot of NEC vs (c) time window and (d) energy window with $200 \mu\text{Ci}$ in the breast. The peak NEC is about 12000 at 2-3 ns time window and ~24% energy window.

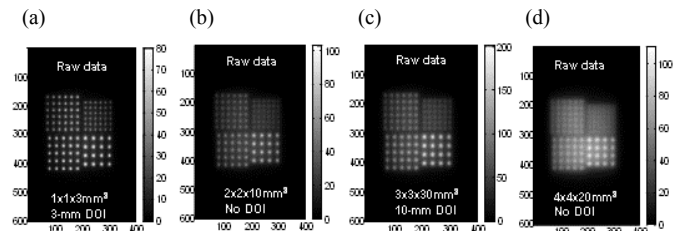


Fig. 7. Tumor visualization without any background activity present. The LSO crystal pixel size is (a), $1 \times 1 \times 3 \text{ mm}^3$ with DOI of 3mm, (b) $2 \times 2 \times 10 \text{ mm}^3$ without DOI, (c) $3 \times 3 \times 30 \text{ mm}^3$ with DOI of 10 mm, and (d) $4 \times 4 \times 20 \text{ mm}^3$ without DOI.

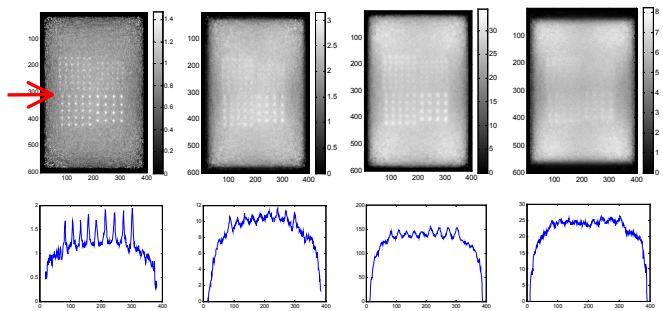


Fig. 8. (Top) Data acquired for 30 seconds, with hot tumors in center plane, warm breast tissue background (10:1 tumor:breast concentration ratio), and 4 cm plate separation for different LSO crystal pixel size, DOI resolution and energy resolution. Images are reconstructed with solid angle and photon attenuation correction. (Bottom) Plots of 1-D profiles through the top row of 3.5 and 4.0 mm diameter tumors as indicated by the arrow in the top left image.

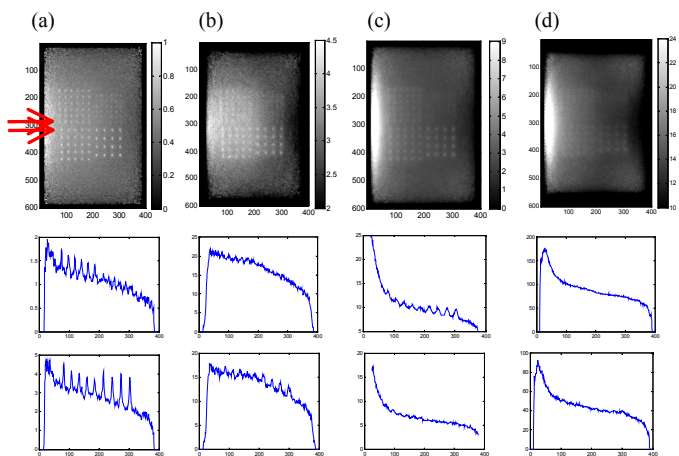


Fig. 9. (Top) Images acquired after on 30 seconds of scanning time with tumor:breast:heart:torso activity ratio of 10:1:10:1, with 4 cm plate separation for different LSO crystal size (see Table 1 and Figure 2b for details). Images are reconstructed with solid angle and photon attenuation correction. The left edge of the images were hotter due to high background activity from heart. (Bottom) Plots of 1-D profiles taken through the bottom row of the 3.0 and 2.5 mm tumors and through the top row of the 3.5 and 4.0 mm diameter tumors as indicated by the arrows in the top left image.

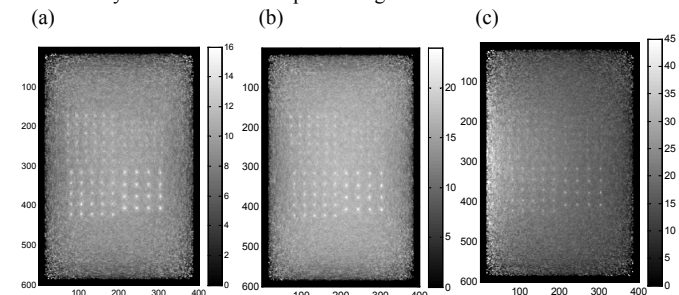


Fig. 10. (Left) with only breast tissue as background, tumor:breast activity concentration ratio is 10:1 and source plane is offset at $x = 1 \text{ cm}$, (middle) with only breast phantom as background and activity concentration ratio is 5:1 and source plane at the $x = 0$, (right) with all background activity of tumor:breast:heart:torso = 10:1:10:1 and panel separation of 8 cm.

IV. DISCUSSION AND CONCLUSIONS

A typical clinical PET system has $> 20\%$ energy resolution of $> 4 \text{ ns}$ time resolution, and $> 6 \text{ mm}$ spatial resolution. This performance along with the bulky geometry makes current

clinical PET systems unsuitable for breast cancer imaging. The recently developed thin flex PSAPD, with coupled LSO crystals, has shown <12% FWHM energy resolution at 511 KeV, around 2 ns FWHM time resolution, and around 1.1 mm FWHM intrinsic spatial resolution [7]. Based on this detector performance, we have proposed to build a dual-panel PET camera dedicated for breast cancer imaging.

In this paper, we simulated the dedicated dual-panel PET camera with different crystal and energy resolutions with a fixed 2 ns time resolution (Table 2) to isolate the effects of crystal size and energy resolution. In practice, the other low energy resolution camera systems may also not be able to achieve the 2 ns time resolution and worse random background effects would result.

Figs. 7, 8, and 9 show that the $1 \times 1 \times 3 \text{ mm}^3$ LSO based PET camera has markedly superior lesion contrast and lesion-to-background ratio. Further, the background is lower than the systems with larger crystal sizes and worse energy resolution. This implies that the improved energy resolution of <12% at 511 KeV helps to enhance the lesion visualization ability of the PET camera. The narrow energy window (24%) was used to help to significantly reduce the scatter and random coincidence events coming mainly from background activity.

We noticed that the lesion visualization ability of the $1 \times 1 \times 3 \text{ mm}^3$ crystal camera is significantly better than for the other crystal sizes. For example, with the 4-mm diameter sources in Fig. 8, the mean peak-to-valley ratio is 1.7 (Fig. 8(a)) compared to 1.2 for the $2 \times 2 \times 10 \text{ mm}^3$ crystal resolution (Fig. 10(b)). Figs. 7, 8, and 9 also show that the superior intrinsic spatial resolution (1 mm in plane, 3 mm DOI) leads to tumor foci that appear brighter and narrower with better separation. The superior energy resolution (12% FWHM) leads to superior tumor-to-background contrast when strong background activity from the adjacent heart and torso are present.

The sensitivity of this dedicated PET camera is significantly higher than the clinical systems. At the center of the FOV, the proposed dual-panel camera has sensitivity of around 14% with an energy window of 350-650 keV and panel separation of 4 cm. A dual-plate system comprising of $1 \times 1 \times 3 \text{ mm}^3$ crystals can resolve 2.5 mm diameter ($8 \mu\text{l}$) tumors in only 30 seconds acquisition time. This is significantly faster compared to existing clinical systems. A short acquisition time could potentially help to increase the cost effectiveness of a dedicated breast imaging PET system by increasing throughput. Alternatively, the high sensitivity could be used to significantly reduce the injected dose applied to the patient, thereby reducing the radiation dosage to the patient.

Our PET camera with $1 \times 1 \times 3 \text{ mm}^3$ LSO crystals and 3 mm DOI yields superior resolution and contrast of minute lesions in the presence of warm body background activity (see Fig. 10). The 12% energy and 2 ns time resolution, allows a narrow energy window setting (24%) to significantly reduce both random and scatter coincidence background. This

improves the lesion contrast resolution, while maintaining high >10% coincidence detection sensitivity at the center.

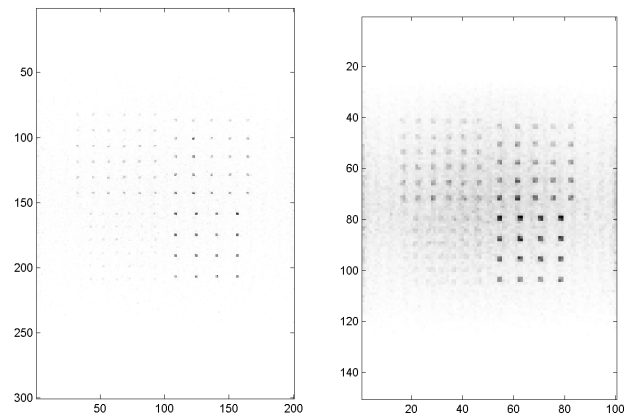


Fig. 11. Shown are OS-EM images with voxel size of (Left) 0.5 and (Right) 1 mm (same data set from Fig. 9, Left). Reconstructed without normalization or attenuation correction.

ACKNOWLEDGEMENT

We thank Dr. Frezghi Habte for useful discussions. This work is supported in part by grant #R21 CA098691 from NIH-NCI.

REFERENCES

- [1] Moses WM and Qi J., Instrumentation optimization for positron emission mammography. *Nucl. Inst. Meth. A*. Vol. 527, pp. 76-82, 2004.
- [2] Weinberg IN, Beylin D, Zavarzin V, Yarnall S, Stepanov PY, Anashkin E, Narayanan D, Dolinsky S, Lauckner K, Adler LP, Positron emission mammography: High resolution biochemical breast imaging. *Technology in Cancer Research and Treatment* 4(1), February 2005, pp. 55-60.
- [3] Qi, J, Kuo C, Huesman RH, Klein GJ, Moses WM, Reutter BW, Comparison of rectangular and dual-planar positron emission mammography scanners. *IEEE Trans. Nucl. Sci.*, vol. 49, pp.2089-2096, 2002.
- [4] Doshi, NK, Shao Y, Silverman RW, Cherry SR., Design and evaluation of an LSO PET detector for breast cancer imaging. *Med. Phys.* Vol. 27(7), pp. 1535-1543, 2000.
- [5] Raylman RR, Majewski S, Wojcik R, Weisengerger AG, Kross B, Popov V and Bishop HA., The potential role of positron emission mammography for detection of breast cancer. A phantom study. *Med. Phys.* Vol. 27(8), pp. 1943-1954, 2000.
- [6] Levin CS, Foudray AMK, Olcott PD, Habte F., Investigation of position sensitive avalanche photodiodes for a new high-resolution PET detector design. *IEEE Trans. Nucl. Sci.*, vol. 51, pp.805-810, 2004.
- [7] Zhang J, Foudray AMK, Olcott PD, Levin CS, "Performance characterization of a novel thin position-sensitive avalanche photodiode for high resolution PET camera", submitted to *IEEE Trans. Nucl. Sci.* (2005).
- [8] Strother SC, Casey ME and Hoffman EJ., Measuring PET scanner sensitivity: Relating count rates to image signal-to-noise ratios using Noise Equivalent Counts. *IEEE Trans. Nucl. Sci.*, vol. 37, pp.783-788, 1990.
- [9] L. Parra and H.H. Barrett, "List-mode likelihood: EM algorithm and image quality estimation demonstrated on 2-D PET," *IEEE Trans. Med. Imaging*, vol.17, pp. 228-235, 1998.